Ultrafast oxidation of refractory organics via PMS activation by Si-O doped biomimetic montmorillonite: Simultaneous enhanced radical/electron transfer pathways and efficient catalytic membrane system

Jiasheng Mao [a], Kexin Yin [a], Yang Zhang [b], Yanan Shang [b], Qian Li [a], Yanwei Li [c], Baoyu Gao [a], Xing Xu [a],*

[a] *Shandong Key Laboratory of Water Pollution Control and Resource Reuse, School of Environmental Science and Engineering, Shandong University, Qingdao 266237, PR China*
[b] *College of Safety and Environmental Engineering, Shandong University of Science and Technology, Qingdao 266590, PR China*
[c] *Environment Research Institute, Shandong University, Qingdao 266237, PR China*

ARTICLE INFO

ABSTRACT

Carbon-based catalysts always rely on graphitized structure, heteroatomic doping, and defect sites as active sites, and still need to solve the problems of low catalytic activity and poor stability. In this work, a Si-O doped carbon-based catalyst with biomimetic montmorillonite (MT) structure (C/Si@MT) was prepared for oxidizing the refractory organic pollutants via peroxymonosulfate (PMS) activation. The C/Si@MT/PMS system exhibited ultrafast oxidation of versatile refractory organics and strong ability to resist interference from environmental matrixes via simultaneously enhancing both radicals and electron transfer process (ETP). The ETP oxidation of versatile pollutants in the C/Si@MT/PMS system were proceeded via the Si-O site as a bridge, with their k_{obs} data positively correlated to the redox parameters (e.g., falling potential, energy gap between C/Si@MT+PMS* and pollutants). In addition, the inert aluminosilicate was removed in C/Si@MT while retaining the lamellar structure for promoting the continuous oxidation of pollutants with high stability in a catalytic membrane.

1. Introduction

Recently, advanced oxidation processes (AOPs) have received extensive attentions towards the oxidation of various refractory organic contaminants, since they could generate large amounts of highly active free radicals (•OH and $SO_4^{•-}$) and with strong oxidation [1–6]. Compared with traditional AOPs technology, persulfate (peroxymonosulfate (PMS) and peroxodisulfate (PDS)) oxidation has attracted increasing attention due to the advantages of producing $SO_4^{•-}$ with high oxidation potential (2.5–3.1 eV), long half-life (30–40 μs), wide pH application range and no iron by-products [2,7–12]. At present, the construction of efficient catalytic system is the main research direction of persulfate oxidation technology, the core of which is the design and synthesis of catalysts with high activity and high stability to fully activate persulfate to produce reactive oxygen species (ROS), so as to achieve actual water and wastewater treatment [2,8,10].

The activation of PMS by transition metal ions (Ni, Co, Mn, Ce, Fe) or metallic oxides has been developed as high-efficient strategy due to the

availability and reuse properties [4,13–20]. Furthermore, metal ions are easily emitted during the metal leaching process, resulting in secondary contamination, severely limiting the development of AOPs for water remediation. At present, many carbon-based catalysts (e.g., graphene, carbon nanotubes, biomass carbon, MOFs and their derivatives, etc.) are also used to activate PMS to achieve efficient degradation of pollutants [9,16,21,22]. However, carbon-based catalysts mainly rely on graphitized structure, heteroatomic doping, defect sites and surface functional groups as active sites, and still need to solve the problems of low catalytic activity and poor stability [17,22–26].

Natural minerals have been extensively used as template agent of catalysts due to the advantages of chemical stability, abundance, low-cost, and ease of recycling [27–31]. Montmorillonite (MT), a type of natural clay mineral with two-dimensional lamellar structure has been traditionally used as a template material for metal oxides catalysts [30, 32–34]. The two-dimensional lamellar structure contains two outer tetrahedral silicon layers and inner octahedral sheet. However, the current literature on montmorillonite activation of PMS almost

---

exclusively reports how to use MT as a carrier to support the transition metal oxides since the aluminosilicate as the basic composition in MT was inert to activate PMS [32,33,35–37], and does not consider how to use MT's own lamellar structure and its silicon element to achieve efficient activation of PMS. There are two aspects of advantages using specific structure of MT and its silicon element. (i) The electronic structure of carbon-based catalysts can be regulated via doping or connecting other heteroatoms with weak electronegativity (such as O, P, S, B and Si, etc) to the carbon-based substrates [38,39]. The active potential barrier of PMS molecules can be reduced to strengthen the generation of free radicals, so as to optimize the adsorption and reaction process of catalytic sites on oxidants [39]. Since the electronegativity of Si-O bond in MT is much weaker than that of N, P, S and B, the preparation of Si-O doped carbon-based catalyst by connecting Si-O bond with carbon-based substrate will help to further improve the catalytic activity of carbon-based catalyst, which has not been reported in the literature. (ii) The lamellar structure of MT is beneficial to the flow of water samples [40–42], which will promote the continuous oxidation of pollutants and catalytic stability in a continuous catalytic system. As a result, how to remove the inert aluminosilicate in MT while retaining the lamellar structure is the key to use MT as an effective catalyst for PMS activation, which would also be important for further fabrication of MT-based catalytic membrane. This was also a highlight that has not been previously reported.

In this work, a Si-O doped carbon catalyst was prepared via the modification of MT by the polydopamine-derived precursor and followed by hydrofluoric acid (HF) etching. As a result, the inert MT structure was removed by HF etching, but the layered structure of MT was retained, and a Si-O doped carbon-based catalyst with biomimetic MT structure (C/Si@MT) was prepared. The oxidation performances towards versatile pollutants by the C/Si@MT via PMS activation as well as its catalytic pathways were determined. The role of Si-O that affected the PMS activation was also analyzed. In addition, a continuous catalytic system by fixing the C/Si@MT as a catalytic membrane was also carried out. The characteristics of C/Si@MT-based membrane and its continuous catalytic performance for various pollutants in various complex water environments were determined.

2. Materials and methods

2.1. Materials and chemicals

The montmorillonite (MT) was obtained from Macklin Biochemical Co., LTD. Other chemicals, eg., $KHSO_5 \cdot 0.5KHSO_4 \cdot 0.5 \ K_2SO_4$ (PMS), N,N-Diethyl-p-phenylenediamine sulfate salt, Na_2SO_4, N,N-dimethylformamide, ethanol (EtOH), tert-butyl alcohol (TBA), D_2O, Nafion perfluorinated resin, hydrochloric acid (HCl), and trans-stilbene were obtained from Sinopharm Chemical Reagent Co. Ltd. The typical pollutants employed in this study, including tetracycline (TC), bisphenol A (BPA), paracetamol (PCM), chlortetracycline (CTC), atrazine (ATZ), p-chlorophenol (CP), metronidazole (MNZ), nitrophenol (NP), nitrobenzene (NB), benzoic acid (BA) were purchased from Sinopharm Chemical Reagent Co. Ltd. The biochar was obtained from Henan Lize environmental protection technology Co., LTD. The polyethersulfone membrane (PES) was obtained from Haiyan New Oriental Plasticizing Co., LTD. The glassy carbon electrode (GCE) was obtained from Shanghai Jinzhan Industrial Technology Co., LTD.

2.2. Fabrication of C/Si@MT and C/Si@MT/membrane

The MT (2.0 g) was dispersed into 100 mL of deionized water after 10 min ultrasonication, and then 400 mg of dopamine (DA) was fully dissolved in the suspension. Afterward, 1 mL of Tris-buffer (1×10^{-3} m, pH = 8.5) was added and stirred 16 h to achieve the polymerization of DA into polydopamine (PDA) on the surface of MT. The suspension was filtered and washed with deionized water for several times, dried at

60 °C under vacuum overnight. The sample was pre-annealed at 400 °C for 2 h under N_2 atmosphere, and named as C/Si@MT pre. The C/Si@MT pre was annealed at 900 °C for 2 h under N_2 atmosphere. The sample was then immersed in the HF (20%) solution (24 h). The suspension was centrifuged and washed with deionized water for several times. Then the sample was immersed in 100 mL 10% HCl for 12 h, centrifuged and washed with deionized water until neutral to obtain the C/Si@MT (Fig. 1a). The control sample without the addition of MT was also prepared by the same procedures, which was mainly based on the carbonized polydopamine (C-PDA).

The C/Si@MT/membrane was fabricated via vacuum filtration of the as-prepared C/Si@MT catalyst onto the PES membrane and dried in a vacuum desiccator at 80 °C for 24 h.

2.3. Experimental procedure

The degradation of TC was conducted by adding 10 mg of C/Si@MT and PMS (1.0 mM) into 100 mL of TC solutions. The TC solution was extracted at designed time interval and filtered by a filter membrane (0.22 μm). The filtrate was added with 0.5 mL of sodium thiosulfate to quench the residual PMS. In addition, the radicals in the C/Si@MT/PMS system were identified by the addition of various scavengers (e.g., TBA, and EtOH). The H_2O was also replaced by D_2O to determine the potential role of singlet oxygen ($^1O_2$) towards TC oxidation in C/Si@MT/PMS system. Oxidation of other pollutants (e.g., BPA, CTC, NP, CP, ATZ, PCM, MNZ) in the C/Si@MT/PMS system was also carried out, and all degradation experiments were conducted at pH 6.0. In addition, continuous degradation of various pollutants by C/Si@MT/membrane and other membrane systems were carried out via a flow through setup driven by self-gravity.

2.4. Characterization and analysis methods

The structure and composition characteristics of C/Si@MT as well as the C/Si@MT/membrane were evaluated by a series of measurements, and the detailed detection procedures were given in Appendix Text S1. Other experimental procedures, e.g., electron paramagnetic resonance (EPR), electrochemical measurements (open circuit potential, and galvanic oxidation system (GOS)), membrane flux, as well as density functional theory (DFT) calculations were given in Appendix Text S2-S7. The detection details for different pollutants were given in Table S1.

3. Results and discussions

3.1. Characterizations of C/Si@MT

The Scanning Electron Microscope (SEM) image of montmorillonite (MT) showed that the size of individual mineral substance was about 12–15 μm (Fig. 1b). The dominated elements in the MT were based on the Si, O and Al, which were ascribed to the aluminosilicate that was composed of an $Al-O_4(OH)_2$ octahedral sheet (O layer) sandwiched between two Si-O tetrahedral sheets (T layer) [43,44]. The bimetallic oxide-based lamellar structure can be observed in Fig. 1c. After the HF etching, the as-prepared catalyst (C/Si@MT) retained the basic structure of montmorillonite based on the SEM and the HADDF-STEM (High Angle Angular Dark Field-Scanning Transmission Electron Microscopy) of the C/Si@MT (Fig. 1d-g), while the elements were significantly changed (Fig. 1h). As shown in Fig. 1i, the C/Si@MT was mainly comprised of C element (83.6%), and it was followed by O (8.34%), N (6.26%) and Si (1.79%). This result indicated that most of the Si components in the MT has been successfully etched. The component of the preserved lamellar structure in the C/Si@MT was also transferred from bimetallic oxides to the Si-doped lamellar carbon structure (Fig. 1i). In contrast, the C-PDA showed irregular carbon framework without the biomimetic lamellar MT structure (Fig. S1). The HADDF-STEM of the C/Si@MT also exhibited that the C/Si@MT was mainly composed of carbon-based
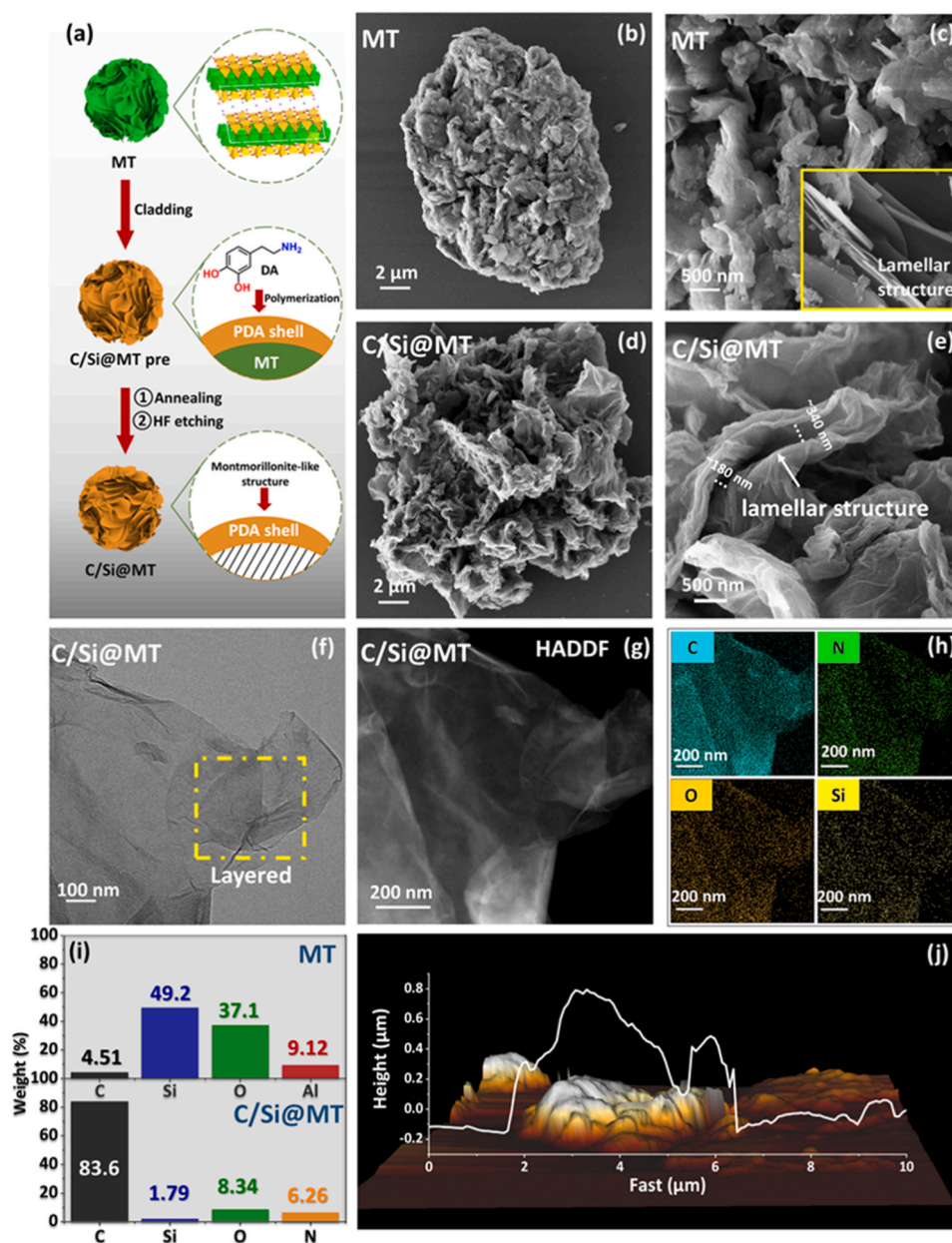
Fig. 1. (a) Fabrication of C/Si@MT from pristine MT. (b) SEM image of MT; (c) Lamellar structure of MT; (d) SEM image of C/Si@MT; (e) Lamellar structure of C/Si@MT; (f) TEM of C/Si@MT; (g) HADDF-STEM of C/Si@MT; (h) TEM mappings of C/Si@MT; (i) Element amounts (C, Si, O, N, Al) in C/Si@MT and pristine MT; (j) AFM of C/Si@MT.

layered structure (Figs. 1g and 1h), doping with Si element derived from the montmorillonite. Atomic force microscope (AFM) showed that the height of the layered structure was approximately 0.2–0.4 μm (Fig. 1j).

XPS C1s of pristine MT and C/Si@MT showed significantly different carbon contents and compositions (Fig. 2a, and Fig. S2)[45,46]. The C atomic content in C/Si@MT accounted for more than 80% of its elemental compositions, which was almost 10 times higher than that (7.1 at%) in pristine MT (Table S2 and S3). What's more, the fraction of C-C in C/Si@MT was significantly higher other C fractions, which indicated the formation of carbon substrates via C-C bonds in the C/Si@MT. In contrast, the atomic content of Si in pristine MT was almost 30-holds higher than that (<1.0 at%) in C/Si@MT (Fig. 2b). In addition, a new peak assigned to the Si-O-C can be observed in the XPS Si 2p of C/Si@MT, which could be attributed to the binding of Si-O with the carbon substrates. The N 1 s of C/Si@MT showed an extreme high graphitic N fraction as compared with that of MT, which was derived

from the introduction of graphitic N in the carbon substrates (Fig. S3). The XRD patterns of pristine MT and C/Si@MT also exhibited the great difference in the constituted materials (Fig. 2c). The XRD pattern of pristine MT indicated that it was composed of standard MT ($Ca_{0.2}(Al, Mg)_2Si_4O_{10}(OH)_2 \cdot 4\,H_2O$, PDF#13–0135) and quartz crystal (PDF#46–1045), while the C/Si@MT mainly consisted of the carbon-based material with the specific PDF card (PDF#99–0057) of graphitized carbon without any standard MT and quartz crystals. This was further confirmed by the Raman spectrum of C/Si@MT (Fig. 2d and Fig. S4), which exhibited high degree of graphitized carbon with the ratio of I_d/I_g at 1.49 [25,47]. As a result, the calcination process promoted the formation of graphitized carbon on the surface of MT, and the silicon-based MT and quartz crystals were eliminated by the subsequent etching with Si-O doped carbon substrate left. In addition, the BET surface areas as well as the pore volumes of pristine MT and C/Si@MT were almost the same (Fig. S5, and Table S4), which further confirmed
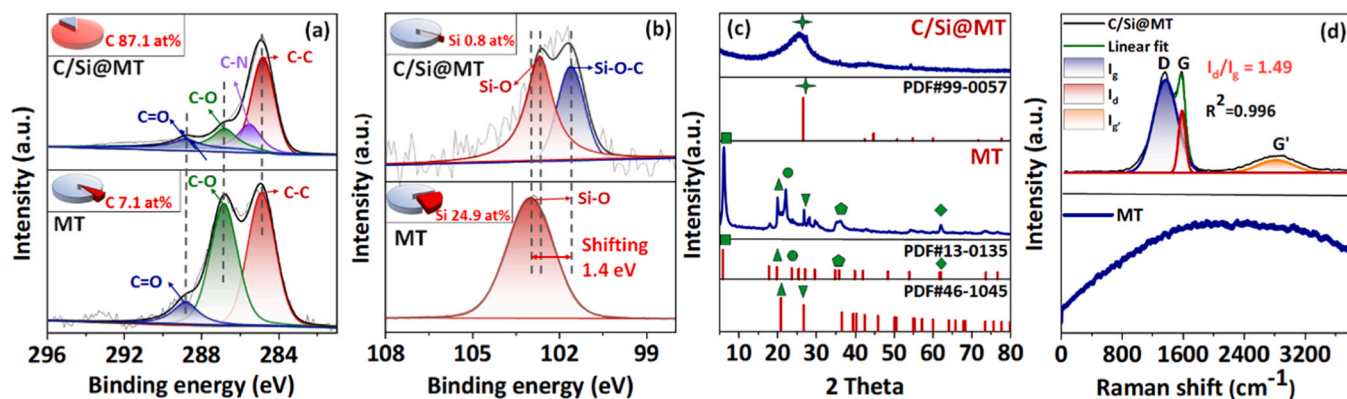
Fig. 2. (a) XPS C1s of pristine MT and C/Si@MT; (b) XPS Si 2p of pristine MT and C/Si@MT; (c) XRD patterns of pristine MT and C/Si@MT; (d) Raman spectra of pristine MT and C/Si@MT (R^2 represented the degree of fit between the peaks and actual results.).
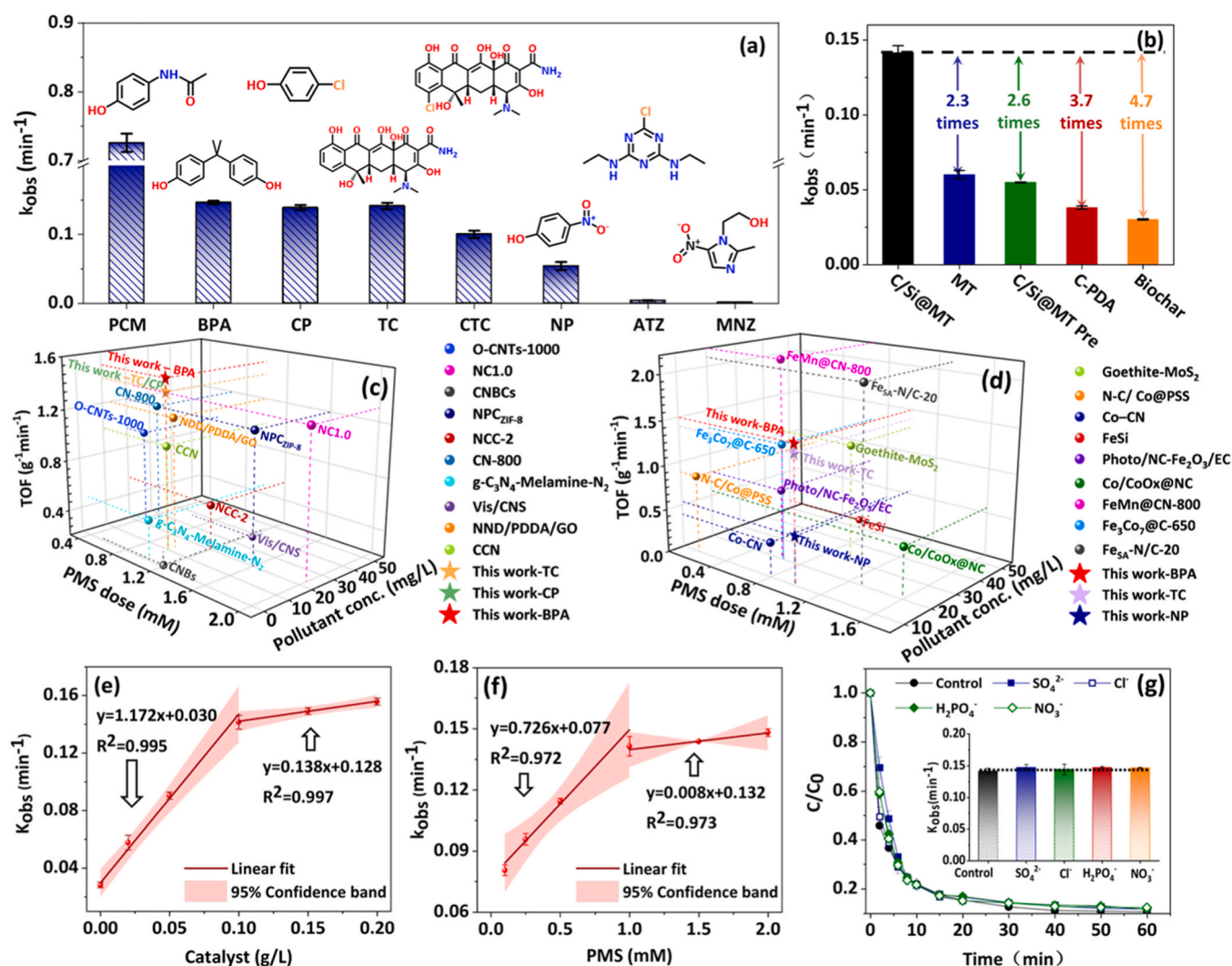

Fig. 3. (a) The k_{obs} data of TC and other pollutants via C/Si@MT/PMS system; (b) TC oxidation by different catalysts (C/Si@MT/PMS, MT, C/Si@MT pre, C-PDA and biochar); The comparison of oxidation capacities towards versatile pollutants by C/Si@MT/PMS with (c) various carbon-based catalysts and (d) metal-based catalysts; (e) Effect of C/Si@MT dosage on the TC degradation; (f) Effect of PMS dosage on the TC degradation; (g) Effect of anions on the degradation of TC in C/Si@MT /PMS systems (Catalyst dosage: 0.1 g/L; PMS dosage: 1.0 mM (except for MNZ and ATZ at PMS of 2.0 mM); Pollutant concentration: 10 mg/L; Anions concentration: 5 mM).

that the C/Si@MT kept the biomimetic MT structure.

3.2. Degradation of TC and other pollutants in C/Si@MT/PMS system

Degradation of TC and other pollutants via C/Si@MT/PMS system was shown in Fig. 3a and Fig. S6. The C/Si@MT could oxidize a broad spectrum of pollutants with different structures via PMS activation (Fig. S7). For example, the ultrafast and complete degradation of PCM within 4 min could be observed in the C/Si@MT/PMS system with the degradation rate (k_{obs}) of 0.728 min^{-1}. The C/Si@MT/PMS system also exhibited high k_{obs} data towards other pollutants (e.g., TC, CTC, BPA, CP, NP). The TC oxidation by other catalysts (e.g., MT, C/Si@MT pre, C-PDA and biochar) was determined (Fig. S8), and the results showed that the k_{obs} of TC oxidation by C/Si@MT/PMS system was 2.3–4.7 times higher than those of other catalysts/PMS systems (Fig. 3b). The comparison of oxidation capacities towards versatile pollutants by C/Si@MT/PMS with various carbon-based catalysts and metal-based catalysts was shown in Figs. 3c and 3d, Table S5 and S6. The C/Si@MT/PMS exhibited extraordinary excellent catalytic performances as compared with those of carbon-based catalysts and even higher than most metal-based catalysts. Effect of C/Si@MT dosage on the TC degradation showed two degradation stages (Fig. 3e and Fig. S9a), including quick degradation process ($k = 1.172$) with C/Si@MT dosage increasing from 0.025 to 0.1 g/L and gentle degradation process ($k = 0.138$) with dosage from 0.1 to 0.2 g/L. Similar phenomenon also occurred in the PMS dosage (Fig. 3f and Fig. S9b), which showed an obvious boundary in the k_{obs} at 1 mM of PMS. The PMS consumption achieved approximately 60% within 60 min (Fig. S10). These results indicated the saturation of catalytic sites in C/Si@MT as well as the consumption of PMS would reach the equilibrium at a certain dosage of PMS (1 mM) and C/Si@MT (0.1 g/L). In addition, the k_{obs} of TC oxidation kept stable under the backgrounds of different anions (Fig. 3g), which indicated its strong ability to resist interference from environmental matrixes. In addition, the oxidation capacity of C/Si@MT was examined in five cyclic TC degradation experiments under the same condition (Fig. S11). The results revealed that the C/Si@MT exhibited good recyclability.

3.3. Degradation mechanism of TC in C/Si@MT/PMS system

The degradation mechanisms of TC in C/Si@MT/PMS system were determined by conducting a series of quenching tests and EPR spectra. TBA is an exclusive probe for HO$^\bullet$ radical with $k_{HO\bullet,TBA}$ of 7.6×10^8 M^{-1}S^{-1}. EtOH can be used the typical scavenger for detecting both the SO$_4^{\bullet-}$ and HO$^\bullet$ [48,49]. As for the C/Si@MT/PMS system, a certain quenching effect can be observed after adding the EtOH and TBA with the k_{obs} value decreasing from 0.143 min^{-1} to 0.116–0.132 min^{-1} (Fig. 4a, and Fig. S12). In contrast, no quenching effect can be observed in MT/PMS, C/Si@MT pre/PMS, and C-PDA/PMS systems (Fig. S12). Increasing the concentrations of EtOH and TBA from 250 mM to 1000 mM also resulted in the slight decrease of k_{obs} (Fig. S13). As a result, both SO$_4^{\bullet-}$ and HO$^\bullet$ contributed to the oxidation of TC C/Si@MT/PMS system (Fig. S14). With the increase of quenchers concentration, the inhibition effects on TC degradation were not obvious (Fig. S13). Such a phenomenon indicated that another nonradical oxidation pathway was overwhelming in the C/Si@MT/PMS system, which offset the quenching effects of radicals on TC degradation. The ATZ and MNZ that were exclusive to the radical oxidation could be oxidized in C/Si@MT/PMS system (Fig. S15, and Fig. 4b), which further indicated the existence of radicals in the C/Si@MT/PMS system. Considering that most carbon-based catalysts always exhibited a nonradical pathway with weak or even negligible radical pathway, C/Si@MT could trigger the large amounts of radicals for the degradation of pollutants, which guaranteed the excellent performance over traditional carbon-based catalysts [50,51]. EPR spectra of the C/Si@MT/PMS system exhibited the signals of DMPO-HO·, as shown in Fig. 4c, and the addition of TC showed a certain weaken in the signals of radicals, which further confirmed the contribution of radicals in the TC
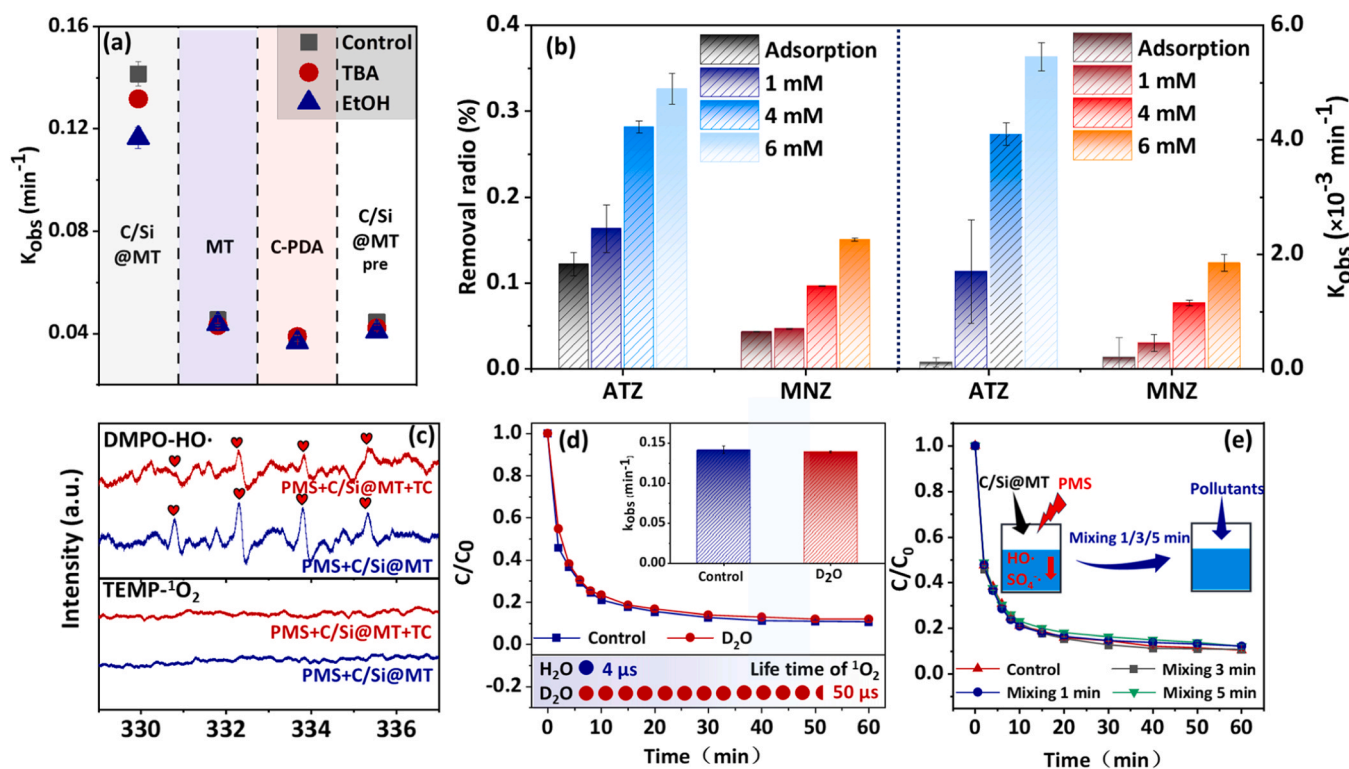

Fig. 4. (a) The k_{obs} values after quenching tests in the C/Si@MT/PMS system; (b) Removal efficiency and k_{obs} of ATZ and MNZ in the C/Si@MT/PMS system; (c) EPR spectra of the C/Si@MT/PMS system; (d) TC oxidation in C/Si@MT/PMS system by using D$_2$O as solution; (e) TC oxidation via a premixture of C/Si@MT and PMS at estimated time intervals. (Catalyst dosage: 0.1 g/L; PMS dosage: 1.0 mM; Pollutant concentration: 10 mg/L; EtOH/TBA concentration: 500 mM).

oxidation. However, no signals of TEMP-$^1O_2$ can be observed in the C/Si@MT/PMS system, which indicated the absence of $^1O_2$ pathway towards TC oxidation; this was also confirmed by the D_2O system, which showed overlapped degradation trend as compared with the H_2O as solution [52,53]. Similarly, no signal of $O_2^{\cdot-}$ can be observed in Fig. S16. This result indicated the absence of $O_2^{\cdot-}$ pathway towards TC oxidation.

The contribution of radicals for oxidating TC in the C/Si@MT/PMS system was further identified by a premixing experiment via premixing the C/Si@MT and PMS at estimated time intervals before adding TC [54, 55]. By premixing PMS and catalyst in the system, radicals were generated instantaneously and defluorated in the catalytic system, a process that resulted in significant consumption of PMS. Therefore, the degradation of pollutants will be affected after the subsequent addition of pollutants. This helps to accurately assess the role of free radicals in the system. If the oxidation mechanism was not dominated by the radicals, the premixture of C/Si@MT and PMS would only cause a minor effect on the TC oxidation [54,55]. Results showed that premixing the C/Si@MT and PMS for 1, 3 and 5 min only showed a very weak inhibition on the TC oxidation (Fig. 4e, and Fig. S17), which indicated that some nonradical (not $^1O_2$) overwhelmed the effect of radicals in oxidating the TC, although large amounts of radicals were produced in

C/Si@MT/PMS system and contributed to the degradation of TC [53].

3.4. Electrochemical analysis of ETP in C/Si@MT/PMS system

A galvanic oxidation system (GOS) was developed to reveal the electron transfer process (ETP) between the TC molecules and metastable C/Si@MT+PMS* considering that the electrons can transfer from the TC molecules to C/Si@MT+PMS* via a electron channel if ETP occurred in the C/Si@MT/PMS system [56]. The C/Si@MT and other catalysts were deposited onto the graphite electrode with superficial area of 28 cm^2, and the oxidant (PMS) and pollutant (TC) were added into two seperated jars via the connection of the agar salt bridge and ampere meter (Fig. 5a and Fig. S18). As showed in Fig. 5b and Fig. S19, the GOS loading with C/Si@MT exhibited the highest maximum current (159.49 μA), and it was followed by MT (25.98 μA), C/Si@MT pre (20.75 μA), C-PDA (17.86 μA), control(15.18 μA). In addition, the equilibrium current (16.72 μA) of C/Si@MT was also higher than those (1.97–4.40 μA) of other catalysts (Fig. 5c). As a result, the doped Si-O in carbon-based biomimetic MT (C/Si@MT) can trigger higher ETP via the electrons transferring from the TC molecules to C/Si@MT+PMS* .

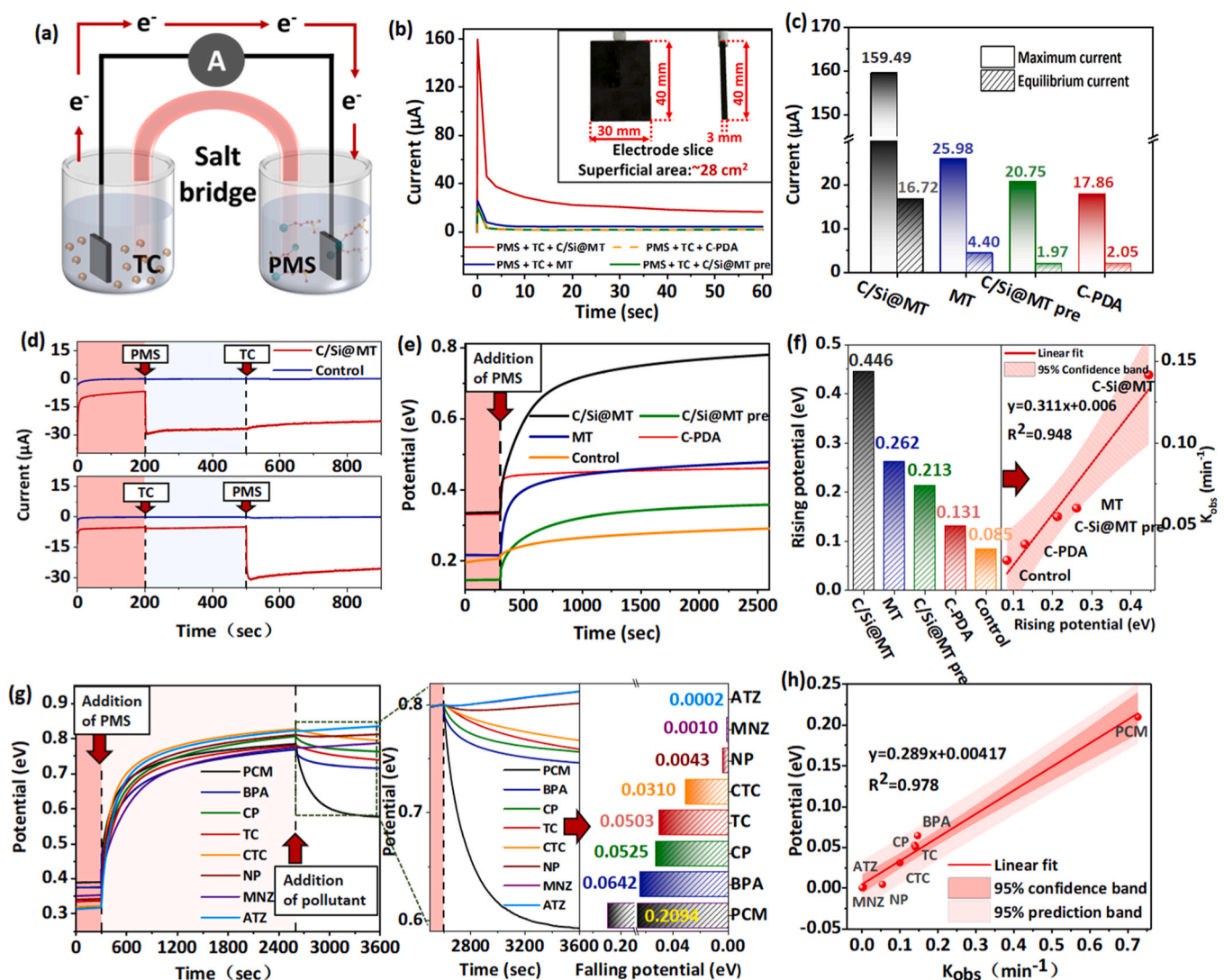To further the unveil ETP in C/Si@MT/PMS system, amperometric i-

Fig. 5. (a) The scheme of GOS; (b) Relative current of GOS coating with C/Si@MT; (c) Maximum current and equilibrium current obtained in different systems; (d) Amperometric i-t curve measurements upon via adjusting the adding sequence of PMS and TC using C/Si@MT as the working electrode; (e) Open-circuit potential of C/Si@MT electrode by adding PMS; (f) Linear correlation between the k_{obs} obtained in different catalyst systems and their rising potentials; (g) Different falling potential trends after adding different pollutants; (h) Linear correlation between the k_{obs} obtained in different pollutants systems and their falling potentials.

t curves were recorded via adjusting the adding sequence of PMS and TC by using C/Si@MT as the working electrode (Fig. 5d). The current density of C/Si@MT electrode was decreased significantly after adding PMS, which may be attributed to the electron redistribution caused by the binding between the PMS and C/Si@MT [19]. In contrast, when TC was first added to the electrochemical system, no electron transfer can be observed between TC and the C/Si@MT. These results demonstrated the formation of substable C/Si@MT+PMS*. In addition, the open-circuit potential of C/Si@MT electrode was increased from 0.33 eV to 0.78 eV (Fig. 5e). In contrast, the rising potential for other catalysts were relatively lower (0.086–0.26 eV). These results showed that the formation of substable C/Si@MT+PMS* could accelerate the potential of C/Si@MT. The linear correlation between the k_{obs} obtained in different catalyst systems and their rising potentials was also calculated (Fig. 5f). The high linear correlation (R^2 =0.948) indicated that C/Si@MT+PMS* could exhibit stronger ETP towards TC oxidation. This phenomenon is also complementary to the result of GOS. In addition, different pollutants were added into the electrochemical C/Si@MT/PMS systems, and three different falling potential trends can be observed (Fig. 5g, and Fig. S20). NP and MNZ showed very negligible potential reduction, while BPA, TC, CP, and CTC exhibited a moderate potential reduction ranging from 0.031 to 0.064 eV. In contrast, superior falling potential (0.21 eV) was observed by adding the PCM in the C/Si@MT/PMS system. The decrease in the open-circuit potential after adding pollutants was due to the redox reaction between pollutants and C/Si@MT+PMS*, resulting the the decomposition of surface complex [18,25,53]. As a result, strong ETP would occur in C/Si@MT/PMS system by adding the pollutants (e.g., PCM), with PMS as electron acceptor and PCM as electron donor. This result can be confirmed by the linear correlation between the k_{obs} obtained in different pollutants systems and their falling potentials, which showed the correlation of $R^2 = 0.977$ (Fig. 5h). The above electrochemical experiments provided compelling evidence for the presence of a strong ETP in C/Si@MT/PMS system. Furthermore, the correlation between the k_{obs} of different pollutant and the decline in open circuit potential substantiated the leading role played by ETP within the system.

3.5. DFT analysis for the oxidation of pollutants in C/Si@MT/PMS system

DFT calculation via the molecular orbital (MO) analysis of C/Si@MT/PMS complexes and pollutants was further used to identify the ETP oxidation in C/Si@MT/PMS system towards different pollutants [57,58]. The premise of ETP oxidation in C/Si@MT/PMS system was based on the electron transfer from the Highest Occupied Molecular Orbital (HOMO) of pollutants to Lowest Unoccupied Molecular Orbital (LUMO) of C/Si@MT/PMS complexes (Fig. S21 and S22). As shown in the Figs. 6a and 6b, different energy gaps occurred between the LUMO of C/Si@MT/PMS complexes (LUMO$_{(C/Si@MT/PMS complexes)}$) and the HOMO of pollutants (HOMO$_{pollutants}$). A lower gap between the LUMO$_{(C/Si@MT/PMS complexes)}$ and HOMO$_{pollutants}$ represented that the electrons migration can be more easily triggered from the pollutants to the C/Si@MT/PMS complexes [53,59], thus accelerating the EPT oxidation towards the targeted pollutants. The calculated gaps also showed well corrections with the lnk_{obs} data (Fig. 6c), which further evidenced that EPT oxidation was dominated in the C/Si@MT/PMS system. In addition, the gap between the LUMO$_{(C/Si@MT/PMS complexes)}$ and HOMO$_{TC}$ was lower than that of LUMO$_{(graphene/PMS complexes)}$-HOMO$_{TC}$, as shown in Fig. 6d. This result further confirmed that the electrons in the TC molecules can be more easily extracted and transferred to the C/Si@MT/PMS complexes via Si-O site as a bridge (Fig. 6e), thus promoting the ETP oxidation of TC in C/Si@MT/PMS system.

3.6. C/Si@MT based catalytic membrane system

Since the ultrafast degradation performance of C/Si@MT towards versatile pollutants via PMS activation, a device integration of C/Si@MT can be developed for the continuous water purification. The C/Si@MT was fixed onto the PES membrane (C/Si@MT/PES) via the vacuum filtration, and a scheme of catalytic membrane system as well as the optical images for the prepared membrane can be seen in Fig. 7a and Fig. S23. AFM of C/Si@MT/PES membrane showed the well deposited C/Si@MT on the surface of PES membrane, and the hight fluctuation of C/Si@MT layer in the range of 0.5–2.0 μm (Figs. 7b and 7c, Fig. S24). This was confirmed by the SEM image of C/Si@MT/PES membrane
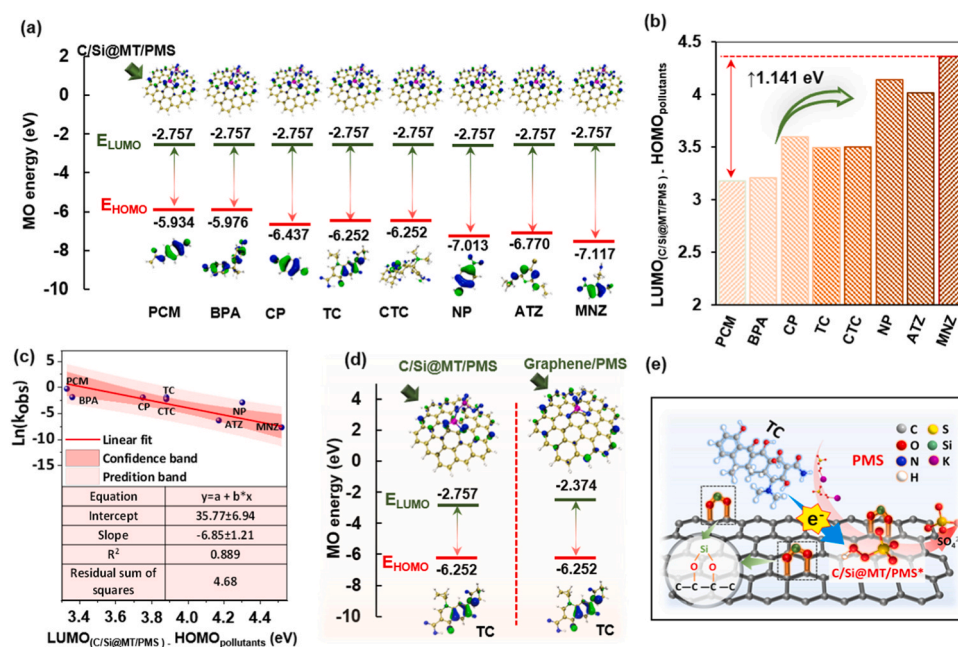

Fig. 6. (a) The LUMO$_{(C/Si@MT/PMS complexes)}$ and HOMO$_{pollutants}$; (b) Different energy gaps between the LUMO$_{(C/Si@MT/PMS complexes)}$ and HOMO$_{pollutants}$; (c) The correction between the calculated gaps and lnk_{obs} data of pollutants; (d) The gap of LUMO$_{(C/Si@MT/PMS complexes)}$-HOMO$_{TC}$ and LUMO$_{(C/Si@MT/PMS complexes)}$-HOMO$_{TC}$; (e) Scheme of ETP oxidation of TC in C/Si@MT/PMS system.
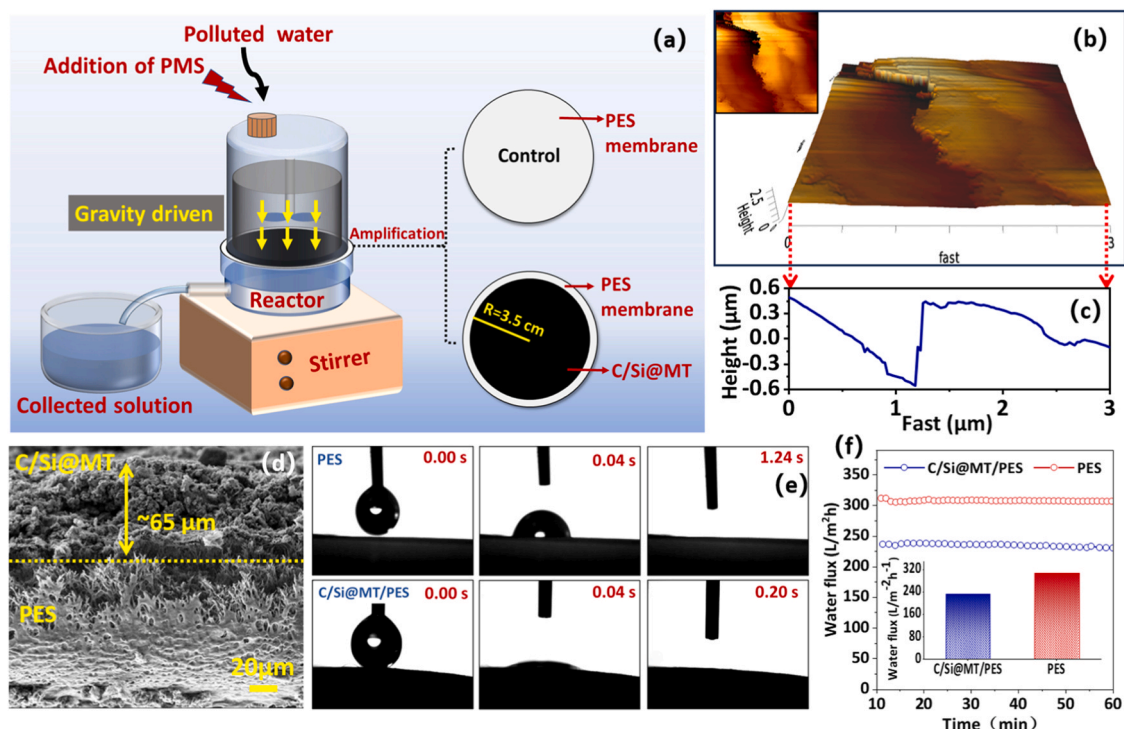
Fig. 7. (a) Scheme of C/Si@MT/PES membrane for continuous oxidation of pollutants; (b) AFM of the C/Si@MT/PES membrane; (c) The height fluctuation of the C/Si@MT/PES membrane; (d) Cross section SEM of C/Si@MT/PES membrane; (e) The contact angle of bare PES membrane and C/Si@MT/PES membrane; (f) Membrane permeate fluxes of C/Si@MT/PES and PES membrane.

(Fig. S25). As a result, The loaded catalysts could provide sufficient active sites for ultrafast oxidation of pollutants in the continuous catalytic system. Cross section SEM image of the C/Si@MT/PES membrane exhibited that the thickness of C/Si@MT layer was ~65 μm (Fig. 7d). The change of hydrophilicity before and after the C/Si@MT desposition on the surface of PES membrane was determined via the contact angle tests [25]. Results showed that the C/Si@MT/PES membrane required a shorter time (<0.20 s) for the drop entirely assimilation as compared with that (<1.24 s) of bare PES membrane (Fig. 7e). This is because (i) the oxygen-containing groups in C/Si@MT could formed more hydrogen bonds with water molecules and promoted the water transport in the pores [4,60]; (ii) the specific biomimetic lamellar MT structure of C/Si@MT would also be beneficial to the flow of water through the C/Si@MT layer. Due to the thickness (~65 μm) of the C/Si@MT layer on the PES membrane, the membrane permeate flux (230 L/(m^2·h)) of C/Si@MT/PES was reduced as compared with that (305 L/(m^2·h)) of bare PES membrane, while it can keep stable with the continuous flow through the C/Si@MT/PES membrane system (Fig. 7f).

The catalytic performances of C/Si@MT/PES membrane towards different pollutants (TC, PCM, BPA, and CP) via PMS activation were shown in Fig. 8a. Continuous 100% degradation of various pollutants can be achieved via the C/Si@MT/PES membrane system with only 80 mg of C/Si@MT deposited on the PES membrane (diameter of 7 cm). In contrast, the bare PES membrane could only uptake approximately 10–40% of pollutants. This result indicated the excellent continuous catalytic activity of C/Si@MT/PES membrane at pH 6.0, although the isoelectric point of the as-prepared membrane at 3.2 (Fig. S26). In addition, the catalytic performances of C/Si@MT/PES membrane towards TC in different water matrixes showed that the as-prepared catalytic membrane could achieve high catalytic capacity in various complex water conditions (Fig. 8b), which was also consistent with the strong ability of C/Si@MT to resist interference from environmental matrixes. As a result, the fabrication of C/Si@MT/PES membrane with multiple oxidation pathways would guarantee the high efficiency and stability of powder catalysts for continuous oxidation, which will be

beneficial for the future designs and fabrications of Fenton-like based equipment (Fig. 8c).

The degradation products of TC as well as their degradation pathways in the C/Si@MT/PMS system were measured and were given in Table S7, Fig. S27 and Fig. 8d. Since the existence of both electron-transfer pathway and radical pathway in the catalytic system, the intermediate products of TC with simultaneous hydroxyl addition (P1-P3) or group fragments breakage (P4-P7) can be observed. The rings of TC can be ultimately attacked and broken into the small fragments (P8, P9, P10). This was also confirmed by the three-dimensional fluorescence (EEM) of the products. As shown in Fig. 8e, the fluorescence intensity of the original TC solution was distributed in the region V (humic acid) containing the aromatic and polycyclic compounds, and their molecular edges were bound to the phenolic hydroxyl, amide, and carboxyl groups [61,62]. The distribution of fluorescence substances in region V was enlarged as the degradation reaction proceeded at 2 and 8 min, which can be attributed to the generation of more intermediate products [63,64]. After 30 min of degradation, most of the fluorescent substances in the TC solution were disappeared, indicating that the TC molecules could be well decomposed in the C/Si@MT/PMS system (Fig. 8e). Meanwhile, a new peak with strong fluorescence intensity can be observed in region V, indicating the generation of intermediate products accompanying the degradation of TC. In addition, the peak had an obvious blue shift in the degradation process, which was due to the reduction of the number of carbonyl, hydroxyl and amine groups. It further indicated that TC was gradually degraded into small molecules. The toxicity analysis of the intermediate products was further determined via the Ecological Structure Activity Relationship (ECOSAR) and the results showed that most of the intermediate products belonged to the "Not harmful" region, which indicated the safety of the C/Si@MT in water-purification applications [64,65]. In addition, the cost was calculated, which indicated that the price was approximately $2.582 per ton of water by using C/Si@MT as a catalyst to purify the wastewater (Table S8).
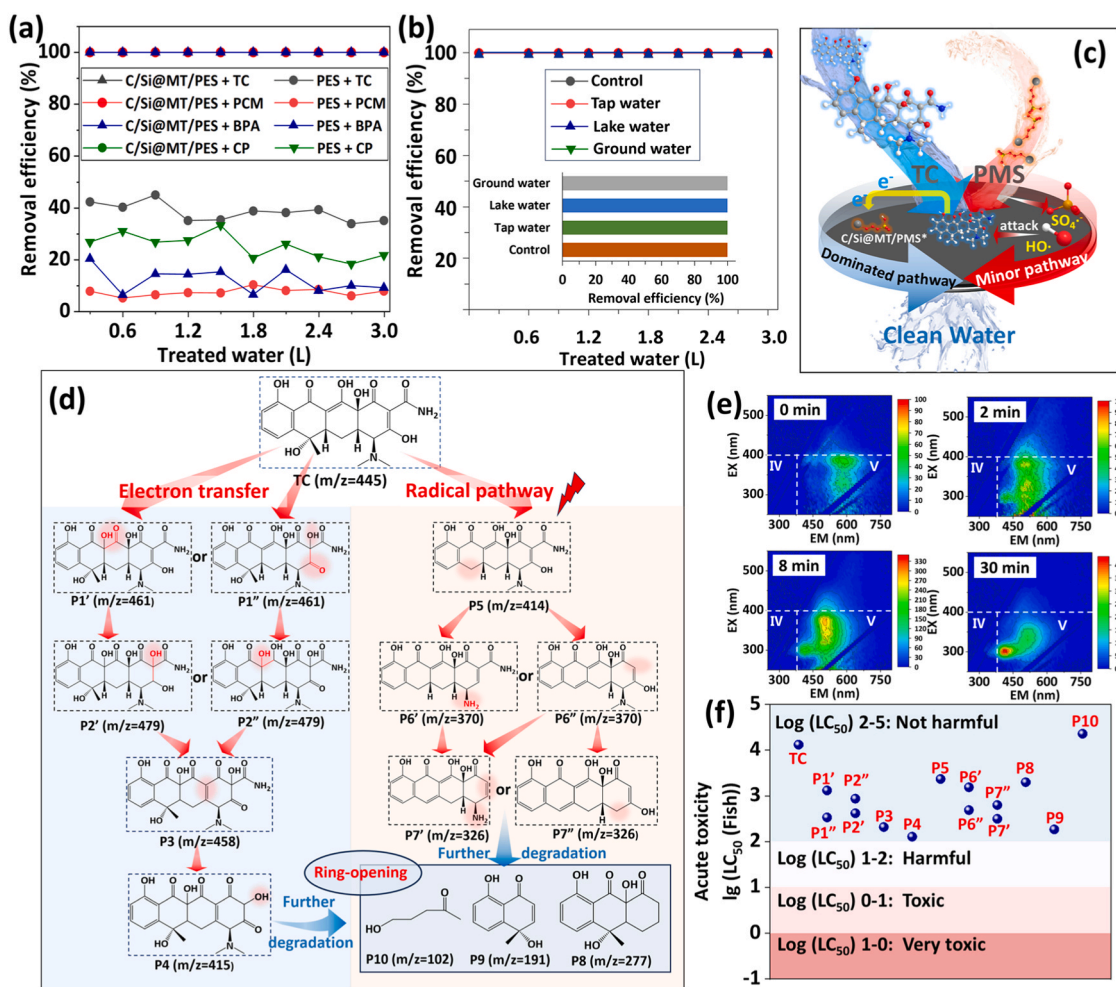
Fig. 8. (a) Catalytic performances of C/Si@MT/PES membrane towards different pollutants (TC, PCM, BPA, and CP) via PMS activation; (b) Catalytic performances of C/Si@MT/PES membrane towards TC in different water matrixes (PMS dosage: 0.5 mM; Pollutant concentration: 0.5 mg/L); (c) Degradation scheme of the C/Si@MT/PES membrane for the continuous flow; (d) Degradation products as well as the degradation pathways; (e) EEM of the TC solution before and after degradation; (f) toxicity analysis of the intermediate products in the C/Si@MT/PMS system.

4. Conclusions

Modulating the Fenton-like activity of carbon-based catalysts always relies on the modulation of various active sites. In this work, we prepared a novel carboncatalyst with specific Si-O doping the carbon-based biomimetic MT structure (C/Si@MT), and used it as a PMS activator for the oxidation of various organic pollutants. The C/Si@MT/PMS system exhibited ultrafast oxidation capacities towards a series of refractory organics with strong anti-interference ability via enhanced radical and ETP pathways. In addition, we first reported that the oxidation capacity of versatile pollutants showed positive correlation ($R^2 = 0.978$) with the reduced potential parameters in the open circuit potentials of C/Si@MT/PMS system after pollutants addition. This was also corresponded well to the corrections between energy gaps of LUMO$_{(C/Si@MT/PMS\ complexes)}$-HOMO$_{pollutants}$ and lnk_{obs} data, which further evidenced that EPT oxidation was dominated in the C/Si@MT/PMS system. We also reported that the C/Si@MT/PES membrane exhibited high membrane permeability and catalytic stability during the continuous degradation of different pollutants, which could be attributed to (i) the formation of more hydrogen bonds with water molecules to promote the water transport in the pores due to the oxygen-containing groups in C/Si@MT, and (ii) the specific biomimetic lamellar MT structure for the flow of water through the C/Si@MT layer. As a result, the fabrication of C/Si@MT/PES membrane with enhanced multiple oxidation pathways would guarantee the high efficiency and stability of powder catalysts for continuous oxidation, which will be beneficial for the future designs and fabrications of Fenton-like based equipment.

CRediT authorship contribution statement

Jiasheng Mao: Methodology, Formal analysis, Investigation, Writing - original draft, Visualization. **Kexin Yin:** Visualization, Methodology. **Yang Zhang:** Formal analysis, Investigation. **Yanan Shang:** Methodology. **Qian Li:** Visualization**:** XASF analysis, DFT calculation. **Yanwei Li:** Formal analysis. **Baoyu Gao:** Supervision. **Xing Xu:** Resources, Writing - review & editing, Supervision.

Declaration of Competing Interest

The authors declare that they have no known competing financial interests or personal relationships that could have appeared to influence the work reported in this paper.

Data availability

Data will be made available on request.

Appendix A. Supporting information

Supplementary data associated with this article can be found in the online version at doi:10.1016/j.apcatb.2023.123428.

References

[1] A. Cai, X. Ling, L. Wang, Q. Sun, S. Zhou, W. Chu, X. Li, J. Deng, Insight into UV-LED/PS/Fe(III) and UV-LED/PMS/Fe(III) for p-arsanilic acid degradation and simultaneous arsenate immobilization, Water Res. 223 (2022), 118989, https://doi.org/10.1016/j.watres.2022.118989.

[2] X. He, K.E. O'Shea, Selective oxidation of H$_1$-antihistamines by unactivated peroxymonosulfate (PMS): Influence of inorganic anions and organic compounds, Water Res. 186 (2020), 116401, https://doi.org/10.1016/j.watres.2020.116401.

[3] J. Sun, L. Liu, F. Yang, A visible-light-driven photocatalytic fuel cell/peroxymonosulfate (PFC/PMS) system using blue TiO$_2$ nanotube arrays (TNA) anode and Cu-Co-WO$_3$ cathode for enhanced oxidation of organic pollutant and ammonium nitrogen in real seawater, Appl. Catal. B: Environ. 308 (2022), 121215, https://doi.org/10.1016/j.apcatb.2022.121215.

[4] Y. Shang, Y. Kan, X. Xu, Stability and regeneration of metal catalytic sites with different sizes in Fenton-like system, Chin. Chem. Lett. 34 (2023), 108278, https://doi.org/10.1016/j.cclet.2023.108278.

[5] Y. Zong, X. Guan, J. Xu, Y. Feng, Y. Mao, L. Xu, H. Chu, D. Wu, Unraveling the overlooked involvement of high-valent cobalt-oxo species generated from the cobalt(II)-activated peroxymonosulfate process, Environ. Sci. Technol. 54 (2020) 16231–16239, https://doi.org/10.1021/acs.est.0c06808.

[6] H. Zhou, J. Peng, X. Duan, H. Yin, B. Huang, C. Zhou, S. Zhong, H. Zhang, P. Zhou, Z. Xiong, Z. Ao, S. Wang, G. Yao, B. Lai, Redox-active polymers as robust electron-shuttle Co-catalysts for fast Fe^{3+}/Fe^{2+} circulation and green fenton oxidation, Environ. Sci. Technol. 57 (2023) 3334–3344, https://doi.org/10.1021/acs.est.2c07447.

[7] L. Wang, Y. Wang, Z. Wang, P. Du, L. Xing, W. Xu, J. Ni, S. Liu, Y. Wang, G. Yu, Q. Dai, Proton transfer triggered in-situ construction of C═N active site to activate PMS for efficient autocatalytic degradation of low-carbon fatty amine, Water Res. 240 (2023), 120119, https://doi.org/10.1016/j.watres.2023.120119.

[8] X. Liu, P. Shao, S. Gao, Z. Bai, J. Tian, Benzoquinone-assisted heterogeneous activation of PMS on Fe$_3$S$_4$ via formation of active complexes to mediate electron transfer towards enhanced bisphenol A degradation, Water Res. 226 (2022), 119218, https://doi.org/10.1016/j.watres.2022.119218.

[9] A. Wang, J. Ni, W. Wang, D. Liu, Q. Zhu, B. Xue, C.-C. Chang, J. Ma, Y. Zhao, MOF derived Co−Fe nitrogen doped graphite carbon@crosslinked magnetic chitosan micro−nanoreactor for environmental applications: Synergy enhancement effect of adsorption−PMS activation, Appl. Catal. B: Environ. 319 (2022), 121926, https://doi.org/10.1016/j.apcatb.2022.121926.

[10] Y. Yao, C. Wang, X. Yan, H. Zhang, C. Xiao, J. Qi, Z. Zhu, Y. Zhou, X. Sun, X. Duan, J. Li, Rational regulation of Co–N–C coordination for high-efficiency generation of ^{1}O$_2$ toward nearly 100% selective degradation of organic pollutants, Environ. Sci. Technol. 56 (2022) 8833–8843, https://doi.org/10.1021/acs.est.2c00706.

[11] C. Bao, H. Wang, C. Wang, X. Zhang, X. Zhao, C.-L. Dong, Y.-C. Huang, S. Chen, P. Guo, X. She, Y. Sun, D. Yang, Cooperation of oxygen vacancy and FeIII/FeII sites in H$_2$-reduced Fe-MIL-101 for enhanced Fenton-like degradation of organic pollutants, J. Hazard. Mater. 441 (2023), 129922, https://doi.org/10.1016/j.jhazmat.2022.129922.

[12] Z. Liu, S. Pan, F. Xu, Z. Wang, C. Zhao, X. Xu, B. Gao, Q. Li, Revealing the fundamental role of MoO$_2$ in promoting efficient and stable activation of persulfate by iron carbon based catalysts: efficient Fe^{2+}/Fe^{3+} cycling to generate reactive species, Water Res 225 (2022), 119142, https://doi.org/10.1016/j.watres.2022.119142.

[13] S. Wang, J. Wang, Single atom cobalt catalyst derived from co-pyrolysis of vitamin B$_{12}$ and graphitic carbon nitride for PMS activation to degrade emerging pollutants, Appl. Catal. B: Environ. 321 (2023), 122051 https://doi.org/10.1016/j.apcatb.2022.122051.

[14] Y. Wang, Y. Wu, Y. Yu, T. Pan, D. Li, D. Lambropoulou, X. Yang, Natural polyphenols enhanced the Cu(II)/peroxymonosulfate (PMS) oxidation: The contribution of Cu(III) and HO•, Water Res. 186 (2020), 116326 https://doi.org/10.1016/j.watres.2020.116326.

[15] Y. Zhao, S. Chen, H. Qie, S. Zhu, C. Zhang, X. Li, W. Wang, J. Ma, Z. Sun, Selective activation of peroxymonosulfate govern by B-site metal in delafossite for efficient pollutants degradation: pivotal role of d orbital electronic configuration, Water Res. 236 (2023), 119957, https://doi.org/10.1016/j.watres.2023.119957.

[16] P. Xu, R. Wei, P. Wang, X. Li, C. Yang, T. Shen, T. Zheng, G. Zhang, CuFe$_2$O$_4$/diatomite actuates peroxymonosulfate activation process: Mechanism for active species transformation and pesticide degradation, Water Res. 235 (2023), 119843, https://doi.org/10.1016/j.watres.2023.119843.

[17] S. Ma, D. Yang, Y. Guan, Y. Yang, Y. Zhu, Y. Zhang, J. Wu, L. Sheng, L. Liu, T. Yao, Maximally exploiting active sites on Yolk@shell nanoreactor: Nearly 100% PMS activation efficiency and outstanding performance over full pH range in Fenton-like reaction, Appl. Catal. B: Environ. 316 (2022), 121594, https://doi.org/10.1016/j.apcatb.2022.121594.

[18] K. Yin, Y. Shang, D. Chen, B. Gao, Q. Yue, X. Xu, Redox potentials of pollutants determining the dominate oxidation pathways in manganese single-atom catalyst (Mn-SAC)/peroxymonosulfate system: selective catalytic mechanisms for versatile pollutants, Appl. Catal. B: Environ. 338 (2023), 123029, https://doi.org/10.1016/j.apcatb.2023.123029.

[19] K. Yin, R. Wu, Y. Shang, D. Chen, Z. Wu, X. Wang, B. Gao, X. Xu, Microenvironment modulation of cobalt single-atom catalysts for boosting both radical oxidation and electron-transfer process in Fenton-like system, Appl. Catal. B: Environ. 329 (2023), 122558, https://doi.org/10.1016/j.apcatb.2023.122558.

[20] Y. Jiang, D. Baimanov, S. Jin, J.C.-F. Law, P. Zhao, J. Tang, J. Peng, L. Wang, K.S.-Y. Leung, W. Sheng, S. Lin, In situ turning defects of exfoliated Ti$_3$C$_2$ MXene into Fenton-like catalytic active sites, Proc. Natl. Acad. Sci. U. S. A. 120 (2022), e2210211120, https://doi.org/10.1073/pnas.2210211120.

[21] Y. Mao, H. Dong, S. Liu, L. Zhang, Z. Qiang, Accelerated oxidation of iopamidol by ozone/peroxymonosulfate (O$_3$/PMS) process: kinetics, mechanism, and simultaneous reduction of iodinated disinfection by-product formation potential, Water Res. 173 (2020), 115615, https://doi.org/10.1016/j.watres.2020.115615.

[22] J. Tan, J. Xu, C. Zhang, Y. Huang, MOFs-derived defect carbon encapsulated magnetic metallic Co nanoparticles capable of efficiently activating PMS to rapidly degrade dyes, Sep. Purif. Technol. 289 (2022), 120812, https://doi.org/10.1016/j.seppur.2022.120812.

[23] C. Guan, J. Jiang, C. Luo, S. Pang, Y. Yang, Z. Wang, J. Ma, J. Yu, X. Zhao, Oxidation of bromophenols by carbon nanotube activated peroxymonosulfate (PMS) and formation of brominated products: comparison to peroxydisulfate (PDS), Chem. Eng. J. 337 (2018) 40–50, https://doi.org/10.1016/j.cej.2017.12.083.

[24] B. Hua, L. Zheng, A. Adeboye, F. Li, Defect- and nitrogen-rich porous carbon embedded with Co NPs derived from self-assembled Co-ZIF-8 @ anionic polyacrylamide network as PMS activator for highly efficient removal of tetracycline hydrochloride from water, Chem. Eng. J. 443 (2022), 136439, https://doi.org/10.1016/j.cej.2022.136439.

[25] K. Yin, L. Peng, D. Chen, S. Liu, Y. Zhang, B. Gao, K. Fu, Y. Shang, X. Xu, High-loading of well dispersed single-atom catalysts derived from Fe-rich marine algae for boosting Fenton-like reaction: role identification of iron center and catalytic mechanisms, Appl. Catal. B: Environ. 336 (2023), 122951, https://doi.org/10.1016/j.apcatb.2023.122951.

[26] W. Ren, L. Xiong, X. Yuan, Z. Yu, H. Zhang, X. Duan, S. Wang, Activation of peroxydisulfate on carbon nanotubes: electron-transfer mechanism, Environ. Sci. Technol. 53 (2019) 14595–14603, https://doi.org/10.1021/acs.est.9b05475.

[27] T. Xie, B. Chen, Y. Mei, S. Feng, X. Tang, W. Xiang, J. Yang, J. He, J. Wang, H. Chen, J. Yang, F. Yang, Ultrafast degradation of tetracycline by PMS activation over perfect cubic configuration MnCo$_2$O$_{4.5}$: new insights into the role of metal-oxygen bonds in PMS activation, Sep. Purif. Technol. 315 (2023), 123694, https://doi.org/10.1016/j.seppur.2023.123694.

[28] X. He, X. Yang, C. Zhang, Y. Xiao, Y. Tang, Catalytic degradation of bisphenol A by heterogeneous bimetal composite carbon in the PMS and H$_2$O$_2$ systems: Performance and mechanism, J. Clean. Prod. 414 (2023), 137571, https://doi.org/10.1016/j.jclepro.2023.137571.

[29] M. Li, H. Zhong, Z. He, L. Hu, W. Sun, P. Loganathan, D. Xiong, Degradation of various thiol collectors in simulated and real mineral processing wastewater of sulfide ore in heterogeneous modified manganese slag/PMS system, Chem. Eng. J. 413 (2021), 127478, https://doi.org/10.1016/j.cej.2020.127478.

[30] S. Yang, P. Wu, J. Liu, M. Chen, Z. Ahmed, N. Zhu, Efficient removal of bisphenol A by superoxide radical and singlet oxygen generated from peroxymonosulfate activated with Fe$_0$-montmorillonite, Chem. Eng. J. 350 (2018) 484–495, https://doi.org/10.1016/j.cej.2018.04.175.

[31] R. Su, N. Li, Z. Liu, X. Song, W. Liu, B. Gao, W. Zhou, Q. Yue, Q. Li, Revealing the generation of high-valent cobalt species and chlorine dioxide in the Co$_3$O$_4$-activated chlorite process: insight into the proton enhancement effect, Environ. Sci. Technol. 57 (2023) 1882–1893, https://doi.org/10.1021/acs.est.2c04903.

[32] J. Wu, G. Cagnetta, B. Wang, Y. Cui, S. Deng, Y. Wang, J. Huang, G. Yu, Efficient degradation of carbamazepine by organo-montmorillonite supported nCoFe$_2$O$_4$-activated peroxymonosulfate process, Chem. Eng. J. 368 (2019) 824–836, https://doi.org/10.1016/j.cej.2019.02.137.

[33] C. Ding, G. Zeng, Y. Tao, X. Long, D. Gong, N. Zhou, R. Zeng, X. Liu, Y. Deng, M.-E. Zhong, Environmental-friendly hydrochar-montmorillonite composite for efficient catalytic degradation of dicamba and alleviating its damage to crops, Sci. Total Environ. 856 (2023), 158917, https://doi.org/10.1016/j.scitotenv.2022.158917.

[34] X.-q Cao, F. Xiao, Z.-w Lyu, X.-y Xie, Z.-x Zhang, X. Dong, J.-x Wang, X.-j Lyu, Y.-z Zhang, Y. Liang, CuFe$_2$O$_4$ supported on montmorillonite to activate peroxymonosulfate for efficient ofloxacin degradation, J. Water Process. 44 (2021), 102359, https://doi.org/10.1016/j.jwpe.2021.102359.

[35] S. Yang, Z. Huang, P. Wu, Y. Li, X. Dong, C. Li, N. Zhu, X. Duan, D.D. Dionysiou, Rapid removal of tetrabromobisphenol A by α-Fe$_2$O$_3$-x@Graphene@ Montmorillonite catalyst with oxygen vacancies through peroxymonosulfate activation: role of halogen and α-hydroxyalkyl radicals, Appl. Catal. B: Environ. 260 (2020), 118129, https://doi.org/10.1016/j.apcatb.2019.118129.

[36] M. Li, Y.-W. Li, P.-F. Yu, H.-M. Zhao, L. Xiang, N.-X. Feng, Q.-K. Li, K.-Y. He, X. Luo, Q.-Y. Cai, S.-Q. Zhou, C.-H. Mo, K.-L. Yeung, Exploring degradation mechanism of tetracycline via high-effective peroxymonosulfate catalysts of montmorillonite hybridized CoFe composites and safety assessment, Chem. Eng. J. 427 (2022), 130930, https://doi.org/10.1016/j.cej.2021.130930.

[37] P. Wang, X. Liu, W. Qiu, F. Wang, H. Jiang, M. Chen, W. Zhang, J. Ma, Catalytic degradation of micropollutant by peroxymonosulfate activation through Fe(III)/Fe (II) cycle confined in the nanoscale interlayer of Fe(III)-saturated montmorillonite, Water Res. 182 (2020), 116030, https://doi.org/10.1016/j.watres.2020.116030.

[38] X. Dong, Z. Chen, A. Tang, D.D. Dionysiou, H. Yang, Mineral modulated single atom catalyst for effective water treatment, Adv. Funct. Mater. 32 (2022), 2111565, https://doi.org/10.1002/adfm.202111565.

[39] Y. Shang, X. Xu, B. Gao, S. Wang, X. Duan, Single-atom catalysis in advanced oxidation processes for environmental remediation, Chem. Soc. Rev. 50 (2021) 5281–5322, https://doi.org/10.1039/D0CS01032D.

[40] Y.-m Sun, L. Feng, L. Yang, Degradation of PCB67 in soil using the heterogenous Fenton process induced by montmorillonite supported nanoscale zero-valent iron, J. Hazard. Mater. 406 (2021), 124305, https://doi.org/10.1016/j.jhazmat.2020.124305.

[41] M. Wu, E. Bi, B. Li, Cotransport of nano-hydroxyapatite and different Cd(II) forms influenced by fulvic acid and montmorillonite colloids, Water Res. 218 (2022), 118511, https://doi.org/10.1016/j.watres.2022.118511.

[42] Y. Nakazawa, T. Abe, Y. Matsui, K. Shinno, S. Kobayashi, N. Shirasaki, T. Matsushita, Differences in removal rates of virgin/decayed microplastics, viruses, activated carbon, and kaolin/montmorillonite clay particles by coagulation, flocculation, sedimentation, and rapid sand filtration during water treatment, Water Res. 203 (2021), 117550, https://doi.org/10.1016/j.watres.2021.117550.

[43] A. Kugler, H. Dong, C. Li, C. Gu, C.E. Schaefer, Y.J. Choi, D. Tran, M. Sprahl, C. P. Higgins, Reductive defluorination of Perfluorooctanesulfonic acid (PFOS) by hydrated electrons generated upon UV irradiation of 3-Indole-acetic-acid in 12-Aminolauric-Modified montmorillonite, Water Res. 200 (2021), 117221, https://doi.org/10.1016/j.watres.2021.117221.

[44] K.J. Rivenbark, M. Wang, K. Lilly, P. Tamamis, T.D. Phillips, Development and characterization of chlorophyll-amended montmorillonite clays for the adsorption and detoxification of benzene, Water Res. 221 (2022), 118788, https://doi.org/10.1016/j.watres.2022.118788.

[45] C. Wang, X. Wang, H. Wang, L. Zhang, Y. Wang, C.-L. Dong, Y.-C. Huang, P. Guo, R. Cai, S.J. Haigh, X. Yang, Y. Sun, D. Yang, Low-coordinated Co-N₃ sites induce peroxymonosulfate activation for norfloxacin degradation via high-valent cobalt-oxo species and electron transfer, J. Hazard. Mater. 455 (2023), 131622, https://doi.org/10.1016/j.jhazmat.2023.131622.

[46] M. Ma, F. Xu, J. Liu, B. Li, Z. Liu, B. Gao, Q. Li, Insights into S-doped iron-based carbonaceous nanocomposites with enhanced activation of persulfate for rapid degradation of organic pollutant, Chemosphere 335 (2023), https://doi.org/10.1016/j.chemosphere.2023.139006.

[47] C. Ding, Z. Liu, S. Pan, C. Zhao, Z. Wang, B. Gao, Q. Li, Activation of peroxydisulfate via Fe@sulfur-doped carbon-supported nanocomposite for degradation of norfloxacin: efficiency and mechanism, Chem. Eng. J. 460 (2023), 141729, https://doi.org/10.1016/j.cej.2023.141729.

[48] G.V. Buxton, C.L. Greenstock, W.P. Helman, A.B. Ross, Critical review of rate constants for reactions of hydrated electrons, hydrogen atoms and hydroxyl radicals (·OH/·O⁻) in aqueous solution, J. Phys. Chem. Ref. Data 17 (1988) 513–886, https://doi.org/10.1063/1.555805.

[49] P. Neta, J. Grodkowski, A.B. Ross, Rate constants for reactions of aliphatic carbon-centered radicals in aqueous solution, J. Phys. Chem. Ref. Data 25 (1996) 709–1050, https://doi.org/10.1063/1.555978.

[50] W. Ren, C. Cheng, P. Shao, X. Luo, H. Zhang, S. Wang, X. Duan, Origins of electron-transfer regime in persulfate-based nonradical oxidation processes, Environ. Sci. Technol. 56 (2022) 78–97, https://doi.org/10.1021/acs.est.1c05374.

[51] W. Ren, L. Xiong, G. Nie, H. Zhang, X. Duan, S. Wang, Insights into the electron-transfer regime of peroxydisulfate activation on carbon nanotubes: the role of oxygen functional groups, Environ. Sci. Technol. 54 (2020) 1267–1275, https://doi.org/10.1021/acs.est.9b06208.

[52] Y. Zong, L. Chen, Y. Zeng, J. Xu, H. Zhang, X. Zhang, W. Liu, D. Wu, Do we appropriately detect and understand singlet oxygen possibly generated in advanced oxidation processes by electron paramagnetic resonance spectroscopy? Environ. Sci. Technol. 57 (2023) 9394–9404, https://doi.org/10.1021/acs.est.3c01553.

[53] M. Yang, Z. Hou, X. Zhang, B. Gao, Y. Li, Y. Shang, Q. Yue, X. Duan, X. Xu, Unveiling the origins of selective oxidation in single-atom catalysis via Co–N₄–C intensified radical and nonradical pathways, Environ. Sci. Technol. 56 (2022) 11635–11645, https://doi.org/10.1021/acs.est.2c01261.

[54] R. Luo, M. Li, C. Wang, M. Zhang, M.A. Nasir Khan, X. Sun, J. Shen, W. Han, L. Wang, J. Li, Singlet oxygen-dominated non-radical oxidation process for efficient degradation of bisphenol A under high salinity condition, Water Res. 148 (2019) 416–424, https://doi.org/10.1016/j.watres.2018.10.087.

[55] M. Zhang, R. Luo, C. Wang, W. Zhang, X. Yan, X. Sun, L. Wang, J. Li, Confined pyrolysis of metal–organic frameworks to N-doped hierarchical carbon for non-radical dominated advanced oxidation processes, J. Mater. Chem. A. 7 (2019) 12547–12555, https://doi.org/10.1039/c9ta02931a.

[56] M. Luo, H. Zhang, P. Zhou, Z. Xiong, B. Huang, J. Peng, R. Liu, W. Liu, B. Lai, Efficient activation of ferrate(VI) by colloid manganese dioxide: Comprehensive elucidation of the surface-promoted mechanism, Water Res. 215 (2022), 118243, https://doi.org/10.1016/j.watres.2022.118243.

[57] Z. Wei, W. Li, D. Zhao, Y. Seo, R. Spinney, D.D. Dionysiou, Y. Wang, W. Zeng, R. Xiao, Electrophilicity index as a critical indicator for the biodegradation of the pharmaceuticals in aerobic activated sludge processes, Water Res. 160 (2019) 10–17, https://doi.org/10.1016/j.watres.2019.05.057.

[58] P. Shao, P. Yu, X. Duan, L. Yang, H. Shi, L. Ding, J. Tian, L. Yang, X. Luo, S. Wang, Potential difference driving electron transfer via defective carbon nanotubes toward selective oxidation of organic micropollutants, Environ. Sci. Technol. 54 (2020) 8464–8472, https://doi.org/10.1021/acs.est.0c02645.

[59] F. Chen, L.-L. Liu, J.-H. Wu, X.-H. Rui, J.-J. Chen, Y. Yu, Single-atom iron anchored tubular g-C₃N₄ catalysts for ultrafast fenton-like reaction: roles of high-valency iron-oxo species and organic radicals, Adv. Mater. 34 (2022), 2202891, https://doi.org/10.1002/adma.202202891.

[60] P. Duan, X. Xu, K. Guo, Q. Yue, B. Gao, Peroxymonosulfate activation on a chainmail catalyst via an electron shuttle mechanism for efficient organic pollutant removal, Appl. Catal. B: Environ. 316 (2022), 121695, https://doi.org/10.1016/j.apcatb.2022.121695.

[61] T. Maqbool, Y. Qin, Q.V. Ly, J. Zhang, C. Li, M.B. Asif, Z. Zhang, Exploring the relative changes in dissolved organic matter for assessing the water quality of full-scale drinking water treatment plants using a fluorescence ratio approach, Water Res 183 (2020), 116125, https://doi.org/10.1016/j.watres.2020.116125.

[62] Y. Cao, L. Yue, Z. Li, Y. Han, J. Lian, H. Qin, S. He, Construction of Sn-Bi-MOF/ Ti₃C₂ Schottky junction for photocatalysis of tetracycline: performance and degradation mechanism, Appl. Surf. Sci. 609 (2023), 155191, https://doi.org/10.1016/j.apsusc.2022.155191.

[63] Z. Wang, Z. Zeng, H. Wang, G. Zeng, P. Xu, R. Xiao, D. Huang, S. Chen, Y. He, C. Zhou, M. Cheng, H. Qin, Bismuth-based metal–organic frameworks and their derivatives: opportunities and challenges, Coord. Chem. Rev. 439 (2021), 213902, https://doi.org/10.1016/j.ccr.2021.213902.

[64] Y. Yu, Z. Xiong, B. Huang, X. Wang, Y. Du, C. He, Y. Liu, G. Yao, B. Lai, Synchronous removal of pharmaceutical contaminants and inactivation of pathogenic microorganisms in real hospital wastewater by electro-peroxone process, Environ. Int. 168 (2022), 107453, https://doi.org/10.1016/j.envint.2022.107453.

[65] X. Wang, Z. Xiong, Z. Shi, H. Zhu, B. Huang, H. Zhang, P. Zhou, Z. Pan, W. Liu, B. Lai, Switching the reaction mechanisms and pollutant degradation routes through active center size-dependent Fenton-like catalysis, Appl. Catal. B: Environ. 329 (2023), 122569, https://doi.org/10.1016/j.apcatb.2023.122569.